Crystallinity Control of the Topological-Insulator Surface $Bi_{85}Sb_{15}(012)$ via Interfacial Engineering for Enhanced Spin-Orbit Torque

H. Y. Poh,[1,2] C. C. I. Ang,[1] G. J. Lim,[1] T. L. Jin,[1] S. H. Lee,[1,2] E. K. Koh,[1,2] F. Poh,[2] and W. S. Lew[1,*]

[1] *School of Physical and Mathematical Sciences, Nanyang Technological University, 21 Nanyang Link, Singapore 637371, Singapore*

[2] *GLOBALFOUNDRIES Singapore Pte. Ltd., 60 Woodlands Industrial Park D St 2, Singapore 738406, Singapore*

(Received 22 November 2022; revised 27 January 2023; accepted 6 February 2023; published 3 March 2023)

Topological insulators demonstrate high charge-spin conversion efficiency due to their spin-momentum locking at the Dirac surface states. However, the surface states are sensitive to disruption caused by exchange coupling when interfaced with a ferromagnet. Here, we demonstrate the use of various nonmagnetic insertion layer materials, Ti, Cu, and Pt, at the Co/Bi-Sb(012) interface to preserve the topological surface state and promote spin-orbit-torque efficiency through the crystallinity control of Bi-Sb(012). For 20-nm-thick Bi-Sb, a spin Hall angle of up to 8.93 is observed with the use of a Pt insertion layer, while it is otherwise negligible for Co/Bi-Sb(012) interfaces. We further explore the enhancement of Bi-Sb(012) crystallinity with increasing Bi-Sb thickness, revealing a rapidly increasing spin-orbit-torque efficiency that gradually saturates above 30 nm. A clear correlation between spin-orbit-torque efficiency and Bi-Sb(012) crystalline size is identified using x-ray diffractometry, establishing the origin of the high spin-orbit efficiency to be the Bi-Sb(012) crystalline orientation. Our work demonstrates the spin-orbit-torque origin in Bi-Sb experimentally and paves the way for the adaptation of topological insulators as a class of low-energy spin source material for spintronics applications.

DOI: 10.1103/PhysRevApplied.19.034012

I. INTRODUCTION

The discovery of spin-orbit torque (SOT) has opened avenues for applied spintronic devices by exploiting electrical and spin manipulation to achieve fast magnetization switching and low power consumption [1–3]. Heavy metals such as Pt, Ta, and W are commonly used as spin sources in ferromagnet–heavy-metal (FM/HM) heterostructures, where spin currents are generated via the spin Hall effect due to strong spin-orbit coupling [4–7]. However, further development of HM-based SOT devices has been limited by the spin Hall angle (<1) [7–11]. Owing to recent advancements, topological insulators (TIs) have gained much attention due to their unique spin-momentum locking and topologically protected surface states [12–17] [see Fig. 1(a)]. Recent works have reported large spin Hall angle, θ_{SH} in several TIs, such as $\theta_{SH} = 3.5$ in Bi_2Se_3, $\theta_{SH} = 18.6$ in Bi_xSe_{1-x}, and $\theta_{SH} \sim 52$ in Bi-Sb/MnGa [17–19]. However, these TIs generally require an epitaxial single-crystalline structure afforded by the molecular-beam epitaxy growth technique. Thus, they are not ideal for integration and mass production in the semiconductor industry. Furthermore, if the TI interfaces directly with a FM, the difference in the work function of the TI and FM shifts the topological surface state below the Fermi energy. The hybridization of these surface states with metal bands will hence destroy the helical spin structure, and the spin-momentum locking will not be preserved [14,20–22]. Therefore, insertion layers such as Ru, Au, Cu, and Ag have been previously used to decouple the direct exchange coupling at the TI/FM interface [23–26]. Besides exchange decoupling, the insertion layer also plays a critical role in influencing the crystallinity of the TIs and consequently affects the SOT performance. Theoretical prediction and angle-resolved photoemission spectroscopy (ARPES) measurements have shown that the Bi-Sb(012) topological surface state has three Dirac cones at the $\bar{\Gamma}$, $\bar{X}$, and $\bar{M}$ points, which are crucial in obtaining strong SOT [17,27,28]. Hence, an insertion layer that promotes a strong Bi-Sb(012) phase is highly desirable.

In this work, we investigate the crystallinity control of Bi-Sb(012) in the magnetic multilayer structure, Ti(1 nm)/Co(5 nm)/[Ti(1 nm), Cu(1 nm), Pt(1 nm)]/Bi-Sb(20 nm)/Ti(1 nm) [Fig. 1(b)], to promote the SOT by utilizing different insertion layers (Ti, Cu, Pt) at the TI/FM interface. The SOT efficiency of these device structures is characterized using the harmonic Hall technique, and crystallinity is determined using x-ray diffractometry. We

*wensiang@ntu.edu.sg

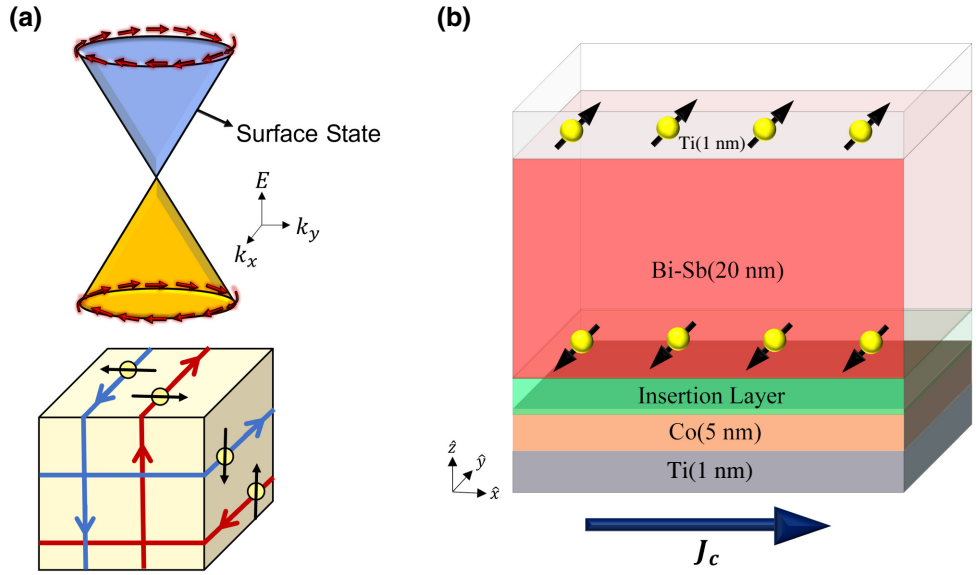

FIG. 1. Electronic band structure of a topological insulator and sample structure. (a) Dirac-like cone of the dispersion at the surface of a topological insulator and real-space interpretation of the surface state of a topological insulator. (b) Schematic structure of Ti/Co/[Ti, Cu, Pt]/Bi-Sb/Ti, where the elements in the square bracket are the different insertion layers.

also extend our work to explore the SOT performance dependence on Bi-Sb thickness from 10 to 100 nm, which reveals further improvement in SOT efficiency that closely correlates to Bi-Sb(012) crystallinity.

II. EXPERIMENTAL DETAILS

The thin-film stacks of Ti(1 nm)/Co(5 nm)/[Cu(1 nm), Ti(1 nm), Pt(1 nm)]/$Bi_{0.85}Sb_{0.15}$(20 nm)/Ti(1 nm), where the square bracket indicates different insertion layers, are deposited on a SiO_2 substrate using dc and rf magnetron sputtering at room temperature. To improve the quality of the Bi-Sb layer, the Bi-Sb is sputtered at a low sputtering rate of 0.059 nm/s using rf magnetron sputtering of 30 W with a base pressure of about 7×10^{-8} Torr, and sputtering pressure of 3×10^{-8} Torr. Upon deposition, the thin films are then patterned into a $5 \times 20\ \mu m^2$ Hall cross structure using a combination of optical lithography and the lift-off technique. The harmonic Hall technique is then carried out on these Hall cross devices to characterize the SOT efficiency. In the harmonic Hall measurement, the first harmonic Hall resistance, R_ω, and second harmonic Hall resistance, $R_{2\omega}$, are obtained with respect to the applied magnetic field, where H_x, the stationary magnetic field of 600 Oe, and H_y, the sweeping magnetic field ranging from −4200 to 4200 Oe, are applied simultaneously. Average ac density, J_{ac} ranging from 2×10^{10} to 3×10^{10} A/m^2 is applied in the $\hat{x}$ direction to determine the dampinglike field, H_D which can be extracted from $R_{2\omega}$ [29,30],

$$R_{2\omega} = \left(\frac{R_A H_D}{2H_s} + R_{\nabla T}\right) X + \frac{R_P H_F}{H_x}(2X^4 - X^2), \quad (1)$$

where R_A is the anomalous Hall resistance, R_P is the planar Hall resistance, $R_{\nabla T}$ is the resistance due to thermal effect, $X = \cos\phi$, where ϕ is the azimuthal angle given by, $\phi = \arctan(H_y/H_x)$, and H_s is the saturation field.

III. RESULTS AND DISCUSSIONS

Figure 2(a) shows the second harmonic Hall resistance, $R_{2\omega}$, with respect to the in-plane sweeping magnetic field across different ranges of current density. The damping-like field, H_D, is extracted using Eq. (1), and the relations between H_D and current density in Bi-Sb, $J_{\text{Bi-Sb}}$, are plotted as shown in Fig. 2(b), where $J_{\text{Bi-Sb}}$ is calculated using the parallel resistor model across the Hall cross structure. The $R_{\nabla T}$ term is found to be negligible from the angular-dependent second-harmonic measurement (see Supplemental Material [31]). θ_{SH} is then given by $\theta_{SH} = (2eM_s t/\hbar)(H_D/J_{\text{Bi-Sb}})$ [32–34], where e is the elementary charge, M_s is the saturation magnetization of the heterostructure, t is thickness of the ferromagnetic layer, and $\hbar$ is the reduced Planck's constant. The θ_{SH} values for Pt, Ti, and Cu insertion layers are 8.93, 7.11, and 8.02, respectively. In contrast, no SOT is observed when the TI is directly adjacent to the ferromagnetic layer and sharing a common interface, as similarly reported in other TI/FM interface studies [24,35]. This observation further verifies the theoretical prediction that the perturbation in the Dirac cone due to the difference in work function between TI and FM will cause a shift in the topological surface state down below the Fermi energy where the hybridization of these surface states with the metal band destroys the TI's

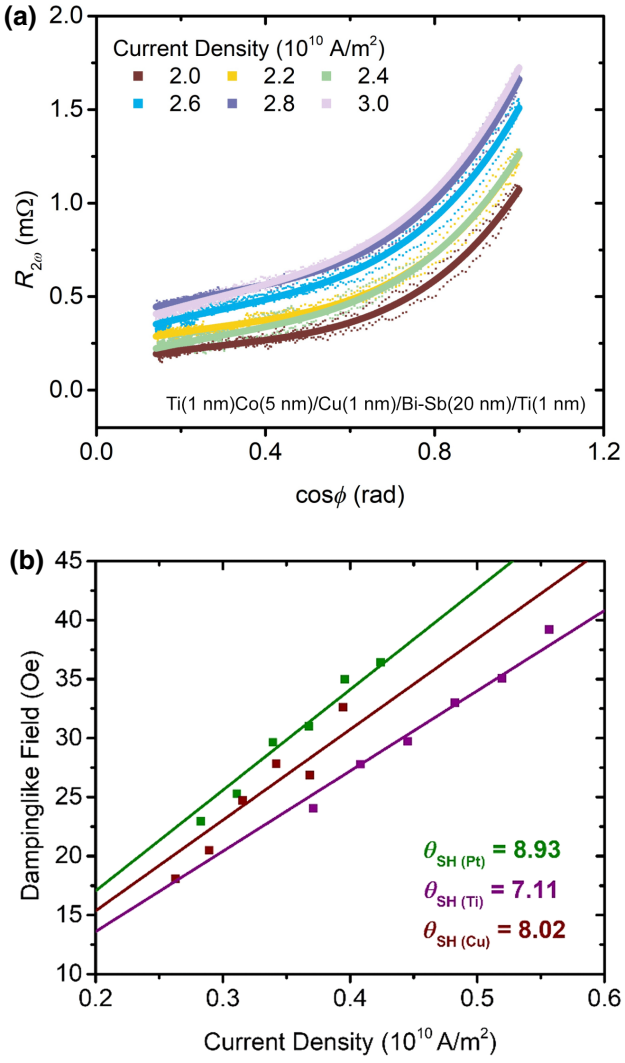

FIG. 2. Dampinglike term characterization by harmonic Hall technique. (a) $R_{2\omega}$ as a function of $\cos\phi$, for average current density ranging from 2 to 3 $\times$ 10^{10} A/m^2. (b) Dampinglike field as a function of current density in Bi-Sb for different insertion layers.

helical spin structure [20,36,37]. The difference in magnitude of θ_{SH} for different insertion layers (Pt, Ti, Cu) can be explained by the crystallinity of Bi-Sb(012) grown above it. Owing to different crystal structures and lattice parameters of the various insertion layers, they promote or impede the growth of the Bi-Sb(012) phase depending on the lattice mismatch between the insertion and Bi-Sb layers. The crystal orientation is crucial, as theoretical prediction and ARPES measurements have shown that Bi-Sb(012) has a topological surface state with three Dirac cones at the $\bar{\Gamma}$, $\bar{X}$, and $\bar{M}$ points [17,27,28], which are beneficial for charge-spin conversion. These Dirac cones on the TI surface are Berry flux monopoles with the same chirality, hence the numbers of Dirac cones are proportional to the total Berry flux, which leads to higher surface spin Hall conductivity [38]. Figure 3(a) shows the x-ray diffraction (XRD) spectra for heterostructures with various insertion layers. The results reveal that at $2\theta = 27.2°$, the peak intensity of Bi-Sb(012) is strongest with the Pt insertion layer, followed by the Cu insertion layer, and the Ti insertion layer. Using the XRD spectra full width half maximum (FWHM) at $2\theta = 27.2°$, the crystalline size can be determined by using the Scherrer equation, $L = K\lambda/\beta\cos\theta$, where L is the crystalline size, K is the Scherrer constant, λ is the wavelength of the x-ray source, and β is the FHWM in radians. The crystalline sizes of Bi-Sb, L, are calculated to be $L = 18.7$, 15.5, and 15.3 nm for Pt, Cu, and Ti insertion layers, respectively, as shown in Fig. 3(b). In addition, all the insertion layers diminish the Bi-Sb(003) peak while improving the Bi-Sb(012)

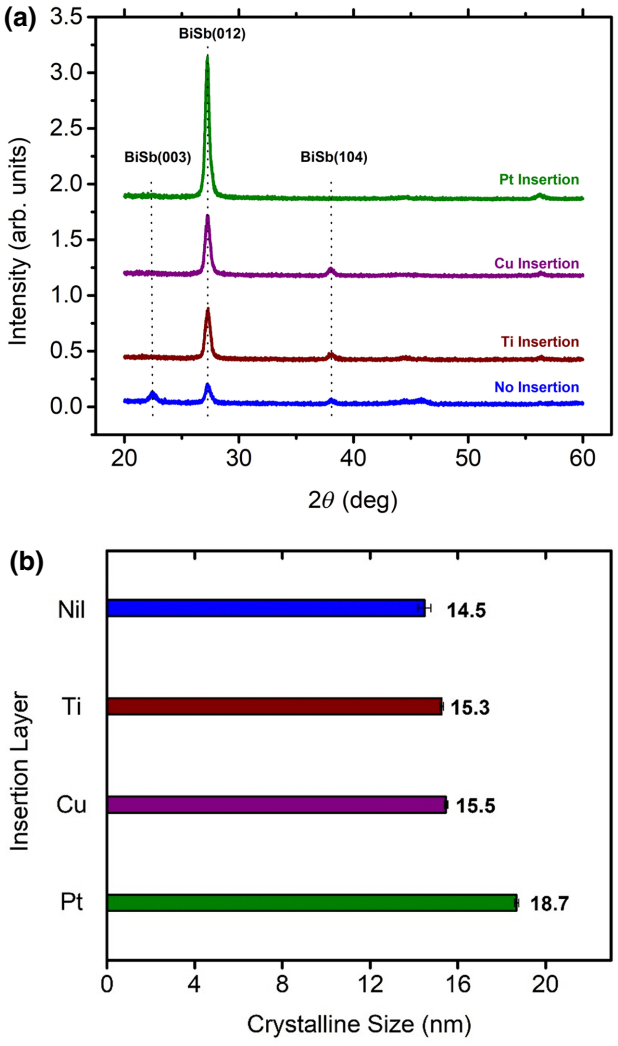

FIG. 3. X-ray diffraction results and crystalline size calculations. (a) XRD $\theta - 2\theta$ spectra for Bi-Sb heterostructure with different insertion layers grown on SiO_2 substrate at $2\theta = 20°-60°$. The peak for Si has been removed for clarity. (b) Crystalline size calculated using Scherrer equation for different insertion layers.

phase. The differences in the crystalline size for different insertion layers may be due to the crystal stress and mismatch at the Bi-Sb and insertion layer interface, as Pt, Cu, and Ti have different crystal structures and dominant phases. Although these insertion layers intermix with the Bi-Sb to form an amorphous layer, the short-range orders of these three different intermixed layers still differ, resulting in different lattice mismatches, hence affecting the crystallinity of the Bi-Sb(012) orientation. The trend in the crystalline size for different insertion layers obtained from the XRD measurement correlates well with the SOT efficiency, further supporting the relation between the crystallinity of Bi-Sb(012) and SOT efficiency. To gain a definitive view on the crystalline structure, high-resolution transmission electron microscopy (HRTEM) is performed on the Ti/Co/Pt/Bi-Sb/Ti structure. Figure 4(a) shows the HRTEM image of the Ti/Co/Pt/Bi-Sb/Ti heterostructure, where highly crystalline Bi-Sb is observed. Owing to the ultrathin layer of Pt, intermixing occurs between the Pt insertion and Bi-Sb layers, which can be seen between the Bi-Sb and Co layers. The sharp interface between the intermixing of the Pt insertion and Bi-Sb, and Bi-Sb layers similarly exhibit good crystalline texture. Using fast Fourier transform, we observe the corresponding electron diffraction pattern as shown in Fig. 4(b). The interplane spacing is determined from the distance from the center

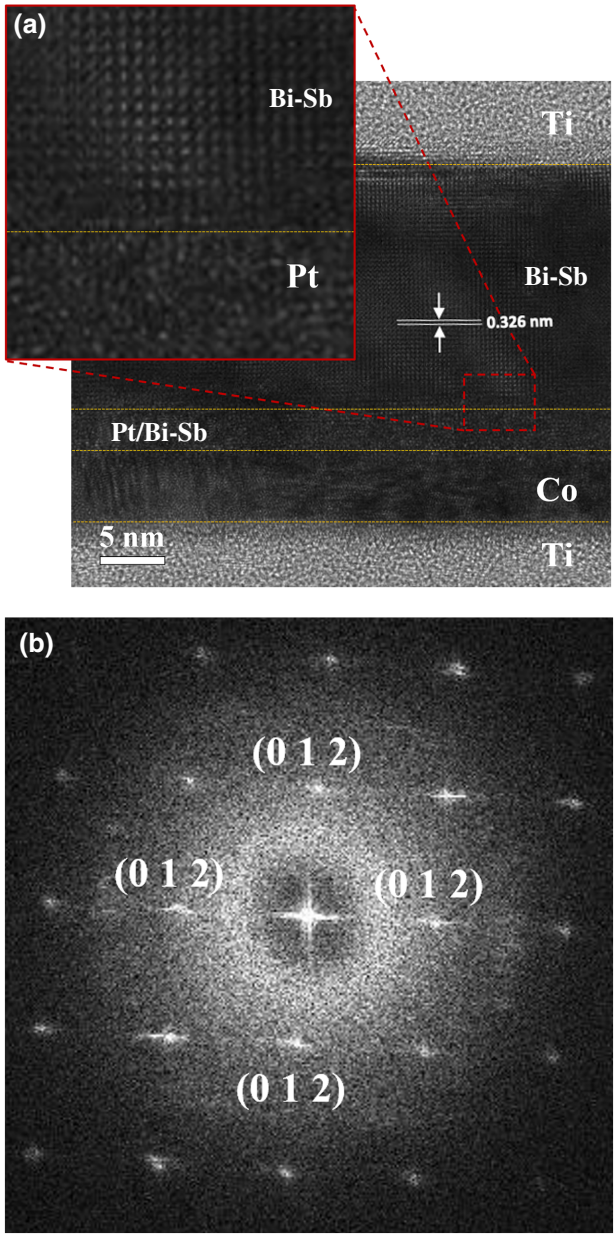

FIG. 4. High-resolution transmission electron microscopy (HRTEM) of Ti/Co/Pt/Bi-Sb/Ti structure. (a) Cross-section TEM images of Ti/Co/Pt/Bi-Sb/Ti. (b) Electronic diffraction pattern using fast Fourier transform.

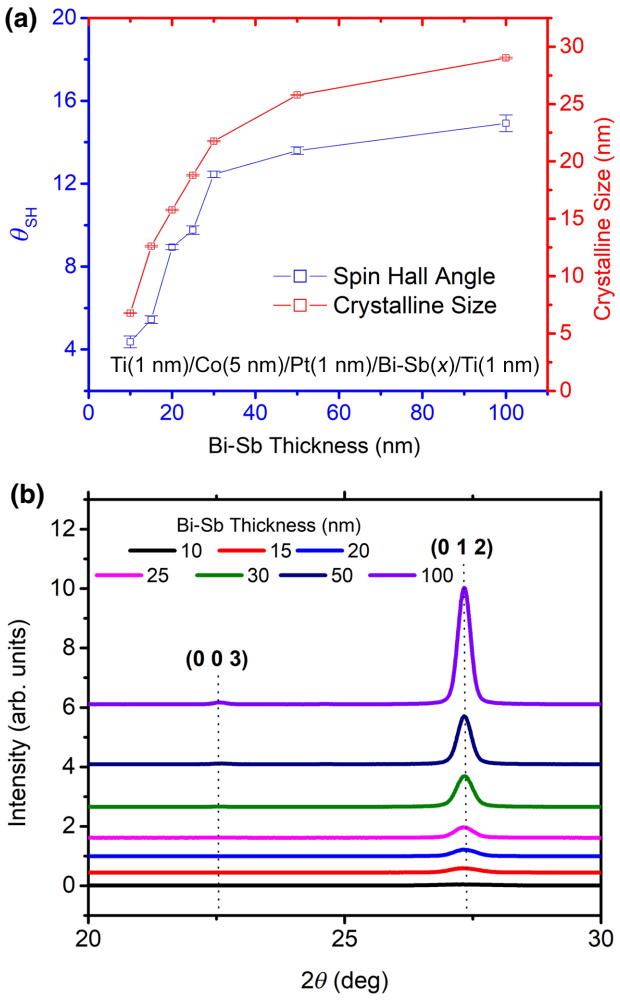

FIG. 5. XRD and spin Hall angle results for varying Bi-Sb thickness. (a) Relation of spin Hall angle and crystalline size as a function of Bi-Sb thickness. (b) XRD $\theta - 2\theta$ spectra for Bi-Sb heterostructure with various Bi-Sb thickness at $2\theta = 20°-30°$.

spots, which correspond to the crystal orientation of Bi-Sb(012). This HRTEM image is thus in good agreement with the XRD results discussed earlier.

The crystal structure of sputter-deposited materials also improves with film thickness. As such, the Bi-Sb thickness dependence ranging from 10 to 100 nm is studied. Hall cross devices of Ti(1 nm)/Co(5 nm)/Pt (1 nm)/Bi-Sb(10−100 nm)/Ti(1 nm) are fabricated and SOT efficiency characterized using the harmonic Hall technique. The relation between θ_{SH} and Bi-Sb thickness is shown in Fig. 5(a), where θ_{SH} shows a similar sharp increase with Bi-Sb thickness and gradually saturates above 30 nm. The corresponding XRD results show a strong Bi-Sb(012) crystallinity with peak intensity increasing significantly with the increase in Bi-Sb thickness, as shown in Fig. 5(b). The crystalline size of Bi-Sb(012) is evaluated using the Scherrer equation and plotted in Fig. 5(a): a rapid increase in the crystalline size from $t_{\text{Bi-Sb}} = 10$ nm to $t_{\text{Bi-Sb}} = 50$ nm, and gradual saturation at $t_{\text{Bi-Sb}} > 50$ nm is observed. As the Bi-Sb thickness increases, the crystal grain tends to become larger and coalesce, leading to the formation of larger grains and/or domains, leading to improvement the Bi-Sb crystallinity [39]. The alignment in the trend of crystalline size and SOT with Bi-Sb thickness is evident, further supporting the attribution of strong SOT to Bi-Sb(012) crystallinity.

IV. CONCLUSIONS

In conclusion, we show that an insertion layer is critical for Bi-Sb SOT generation and the SOT performance depends on the Bi-Sb(012) crystallinity, which is promoted by the insertion layer, with Pt being the optimal material in this study, achieving θ_{SH} of 8.93, compared with Cu and Ti. The crystallinity of Bi-Sb(012) is further improved by increasing Bi-Sb thickness, resulting in the increase of θ_{SH} up to 14.91. A clear correlation between the SOT efficiency and the Bi-Sb(012) crystalline size is observed, hence providing the experimental verification for the Bi-Sb(012) crystalline orientation being the crucial contributor to SOT generation in Bi-Sb.

ACKNOWLEDGMENT

This work was supported by a RIE2020 ASTAR AME IAF-ICP grant (Grant No. I1801E0030) and EDB-IPP: Economic Development Board – Industrial Postgraduate Program (Grant No. RCA-2019-1376).

[1] X. Fan, H. Celik, J. Wu, C. Ni, K.-J. Lee, V. O. Lorenz, and J. Q. Xiao, Quantifying interface and bulk contributions to spin–orbit torque in magnetic bilayers, Nat. Commun. **5**, 3042 (2014).

[2] S. Woo, M. Mann, A. Tan, L. Carreta, and G. Beach, in *2015 IEEE Int. Magn. Conf.* (2015), pp. 1.

[3] S. Fukami, C. Zhang, S. DuttaGupta, A. Kurenkov, and H. Ohno, Magnetization switching by spin–orbit torque in an antiferromagnet–ferromagnet bilayer system, Nat. Mater. **15**, 535 (2016).

[4] Q. Y. Wong, C. Murapaka, W. C. Law, W. L. Gan, G. J. Lim, and W. S. Lew, Enhanced Spin-Orbit Torques in Rare-Earth Pt/$[Co/Ni]_2$/Co/Tb Systems, Phys. Rev. Appl. **11**, 024057 (2019).

[5] C. Hahn, G. De Loubens, O. Klein, M. Viret, V. V. Naletov, and J. Ben Youssef, Comparative measurements of inverse spin Hall effects and magnetoresistance in YIG/Pt and YIG/Ta, Phys. Rev. B **87**, 174417 (2013).

[6] Z. Xu, G. D. H. Wong, J. Tang, E. Liu, W. Gan, F. Xu, and W. S. Lew, Large spin Hall angle enhanced by nitrogen incorporation in Pt films, Appl. Phys. Lett. **118**, 62406 (2021).

[7] H. Y. Poh, C. C. I. Ang, T. L. Jin, F. N. Tan, G. J. Lim, S. Wu, F. Poh, and W. S. Lew, Continuous film spin-orbit torque characterization via four probe measurement, Appl. Phys. Lett. **121**, 12405 (2022).

[8] M. Akyol, B. Kıvrak, K. U. Tümen, and A. Ekicibil, Effect of Ta insertion between Pt and CoFeB on interfacial magnetic anisotropy in Pt/CoFeB/MgO multilayer thin-film stack, J. Mater. Sci. Mater. Electron. **31**, 23037 (2020).

[9] J. Han and L. Liu, Topological insulators for efficient spin-orbit torques, APL Mater. **9**, 60901 (2021).

[10] C.-F. Pai, M. Mann, A. J. Tan, and G. S. D. Beach, Determination of spin torque efficiencies in heterostructures with perpendicular magnetic anisotropy, Phys. Rev. B **93**, 144409 (2016).

[11] I. M. Miron, G. Gaudin, S. Auffret, B. Rodmacq, A. Schuhl, S. Pizzini, J. Vogel, and P. Gambardella, Current-driven spin torque induced by the Rashba effect in a ferromagnetic metal layer, Nat. Mater. **9**, 230 (2010).

[12] L. Fu, C. L. Kane, and E. J. Mele, Topological Insulators in Three Dimensions, Phys. Rev. Lett. **98**, 106803 (2007).

[13] H. Zhang, C. X. Liu, X. L. Qi, X. Dai, Z. Fang, and S. C. Zhang, Topological insulators in Bi_2Se_3, Bi_2Te_3 and Sb_2Te_3 with a single Dirac cone on the surface, Nat. Phys. **5**, 438 (2009).

[14] N. Roschewsky, E. S. Walker, P. Gowtham, S. Muschinske, F. Hellman, S. R. Bank, and S. Salahuddin, Spin-orbit torque and Nernst effect in Bi-Sb/Co heterostructures, Phys. Rev. B **99**, 195103 (2019).

[15] J. Sasaki, H. H. Huy, N. H. D. Khang, P. N. Hai, Q. Le, B. York, X. Liu, S. Le, C. Hwang, M. Ho, and H. Takano, Improvement of the effective spin Hall angle by inserting an interfacial layer in sputtered BiSb topological insulator (bottom)/ferromagnet with in-plane magnetization, IEEE Trans. Magn. **58**, 1 (2022).

[16] S. O. Valenzuela and M. Tinkham, Direct electronic measurement of the spin Hall effect, Nature **442**, 176 (2006).

[17] N. H. D. Khang, Y. Ueda, and P. N. Hai, A conductive topological insulator with large spin Hall effect for ultralow power spin–orbit torque switching, Nat. Mater. **17**, 808 (2018).

[18] M. Dc, R. Grassi, J. Y. Chen, M. Jamali, D. Reifsnyder Hickey, D. Zhang, Z. Zhao, H. Li, P. Quarterman, *et al.*,

Room-temperature high spin–orbit torque due to quantum confinement in sputtered Bi_xSe_{1-x} films, Nat. Mater. **17**, 800 (2018).

[19] A. R. Mellnik, J. S. Lee, A. Richardella, J. L. Grab, P. J. Mintun, M. H. Fischer, A. Vaezi, A. Manchon, E. A. Kim, N. Samarth, and D. C. Ralph, Spin-transfer torque generated by a topological insulator, Nature **511**, 449 (2014).

[20] J. Zhang, J. P. Velev, X. Dang, and E. Y. Tsymbal, Band structure and spin texture of $Bi_2Se_3$3d ferromagnetic metal interface, Phys. Rev. B **94**, 014435 (2016).

[21] J. C. Rojas-Sánchez, S. Oyarzún, Y. Fu, A. Marty, C. Vergnaud, S. Gambarelli, L. Vila, M. Jamet, Y. Ohtsubo, A. Taleb-Ibrahimi, *et al.*, Spin to Charge Conversion at Room Temperature by Spin Pumping into a New Type of Topological Insulator: α-Sn Films, Phys. Rev. Lett. **116**, 96602 (2016).

[22] P. Noel, C. Thomas, Y. Fu, L. Vila, B. Haas, P. H. Jouneau, S. Gambarelli, T. Meunier, P. Ballet, and J. P. Attané, Highly Efficient Spin-to-Charge Current Conversion in Strained HgTe Surface States Protected by a HgCdTe Layer, Phys. Rev. Lett. **120**, 167201 (2018).

[23] H. He, L. Tai, D. Wu, H. Wu, A. Razavi, K. Wong, Y. Liu, and K. L. Wang, Enhancement of spin-to-charge conversion efficiency in topological insulators by interface engineering, APL Mater. **9**, 71104 (2021).

[24] E. Longo, M. Belli, M. Alia, M. Rimoldi, R. Cecchini, M. Longo, C. Wiemer, L. Locatelli, P. Tsipas, A. Dimoulas, *et al.*, Large spin-to-charge conversion at room temperature in extended epitaxial Sb_2Te_3 topological insulator chemically grown on silicon, Adv. Funct. Mater. **32**, 2109361 (2022).

[25] S. Shi, A. Wang, Y. Wang, R. Ramaswamy, L. Shen, J. Moon, D. Zhu, J. Yu, S. Oh, Y. Feng, and H. Yang, Efficient charge-spin conversion and magnetization switching through the Rashba effect at topological-insulator/Ag interfaces, Phys. Rev. B **97**, 41115 (2018).

[26] K. T. Yamamoto, Y. Shiomi, K. Segawa, Y. Ando, and E. Saitoh, Universal scaling for the spin-electricity conversion on surface states of topological insulators, Phys. Rev. B **94**, 24404 (2016).

[27] J. C. Y. Teo, L. Fu, and C. L. Kane, Surface states and topological invariants in three-dimensional topological insulators: Application to $Bi_{1-x}Sb_x$, Phys. Rev. B **78**, 45426 (2008).

[28] X. G. Zhu, M. Stensgaard, L. Barreto, W. S. E. Silva, S. Ulstrup, M. Michiardi, M. Bianchi, M. Dendzik, and P. Hofmann, Three Dirac points on the (110) surface of the topological insulator $Bi_{1-x}Sb_x$, New J. Phys. **15**, 0 (2013).

[29] H. Y. Poh, C. C. I. Ang, W. L. Gan, G. J. Lim, and W. S. Lew, Direct spin accumulation quantification in ferromagnetic heterostructures using DC bias harmonic Hall measurement, Phys. Rev. B **104**, 224416 (2021).

[30] F. Luo, S. Goolaup, W. C. Law, S. Li, F. Tan, C. Engel, T. Zhou, and W. S. Lew, Simultaneous determination of effective spin-orbit torque fields in magnetic structures with in-plane anisotropy, Phys. Rev. B **95**, 174415 (2017).

[31] See Supplemental Material at http://link.aps.org/supplemental/10.1103/PhysRevApplied.19.034012 for the measurement of parasitic effect [40–43].

[32] C. Engel, S. Goolaup, F. Luo, and W. S. Lew, Quantitative characterization of spin-orbit torques in Pt/Co/Pt/Co/Ta/BTO heterostructures due to the magnetization azimuthal angle dependence, Phys. Rev. B **96**, 054407 (2017).

[33] T. Jin, G. J. Lim, H. Y. Poh, S. Wu, F. Tan, and W. S. Lew, Spin reflection-induced field-free magnetization switching in perpendicularly magnetized MgO/Pt/Co heterostructures, ACS Appl. Mater. Interfaces **14**, 9781 (2022).

[34] T. Jin, W. C. Law, D. Kumar, F. Luo, Q. Y. Wong, G. J. Lim, X. Wang, W. S. Lew, and S. N. Piramanayagam, Enhanced spin–orbit torque efficiency in Pt/Co/Ho heterostructures via inserting Ho layer, APL Mater. **8**, 111111 (2020).

[35] E. Longo, L. Locatelli, M. Belli, M. Alia, A. Kumar, M. Longo, M. Fanciulli, and R. Mantovan, Spin-charge conversion in $Fe/Au/Sb_2Te_3$ heterostructures as probed by spin pumping ferromagnetic resonance, Adv. Mater. Interfaces **8**, 2101244 (2021).

[36] P. B. Ndiaye, C. A. Akosa, M. H. Fischer, A. Vaezi, E. A. Kim, and A. Manchon, Dirac spin-orbit torques and charge pumping at the surface of topological insulators, Phys. Rev. B **96**, 014408 (2017).

[37] Y. T. Hsu, K. Park, and E. A. Kim, Hybridization-induced interface states in a topological-insulator-ferromagnetic-metal heterostructure, Phys. Rev. B **96**, 235433 (2017).

[38] T. Shirokura, K. Yao, Y. Ueda, and P. N. Hai, Origin of the Giant Spin Hall Effect in BiSb Topological Insulator, ArXiv:1810.10840 2 (2018).

[39] D. Sadek, R. Daubriac, C. Durand, R. Monflier, Q. Gravelier, A. Proietti, F. Cristiano, A. Arnoult, and S. R. Plissard, Structural and electrical characterizations of BiSb topological insulator layers epitaxially integrated on GaAs, Cryst. Growth Des. **22**, 5081 (2022).

[40] C. O. Avci, K. Garello, M. Gabureac, A. Ghosh, A. Fuhrer, S. F. Alvarado, and P. Gambardella, Interplay of spin-orbit torque and thermoelectric effects in ferromagnet/normal-metal bilayers, Phys. Rev. B **90**, 1 (2014).

[41] Y. Du, R. Thompson, M. Kohda, and J. Nitta, Origin of spin-orbit torque in CoFeB single-layer CoFeB investigated via in-plane harmonic Hall measurements, AIP Adv. **11** (2021).

[42] M. G. Kang, J. G. Choi, J. Jeong, J. Y. Park, H. J. Park, T. Kim, T. Lee, K. J. Kim, K. W. Kim, J. H. Oh, *et al.*, Electric-field control of field-free spin-orbit torque switching via laterally modulated Rashba effect in $Pt/Co/AlO_x$ structures, Nat. Commun. **12**, 8 (2021).

[43] S. Lee, M. G. Kang, D. Go, D. Kim, J. H. Kang, T. Lee, G. H. Lee, J. Kang, N. J. Lee, Y. Mokrousov, *et al.*, Efficient conversion of orbital Hall current to spin current for spin-orbit torque switching, Commun. Phys. **4**, 3 (2021).